IET Electric Power Applications

Research Article

ISSN 1751-8660
Received on 9th April 2019
Revised 17th June 2019
Accepted on 4th July 2019
E-First on 27th September 2019
doi: 10.1049/iet-epa.2019.0309
www.ietdl.org

Data-driven online temperature compensation for robust field-oriented torque-controlled induction machines

Pieter Nguyen Phuc[1,2] ✉, *Hendrik Vansompel*[1,2], *Dimitar Bozalakov*[1,2], *Kurt Stockman*[1,2], *Guillaume Crevecoeur*[1,2]

[1] *EEDT, Flanders Make, Belgium*

[2] *Department of Electrical Energy, Metals, Mechanical Constructions and Systems, Faculty of Engineering and Architecture, Ghent University, Tech Lane Ghent Building 131, 9052 Ghent, Belgium*

✉ *E-mail: Pieter.NguyenPhuc@UGent.be*

Abstract: Squirrel-cage induction machines (IMs) with indirect field-oriented control are widely used in industry and are frequently chosen for their accurate and dynamic torque control. During operation, however, temperature rises leading to changes in machine parameters. The rotor resistance, in particular, alters, affecting the accuracy of the torque control. The authors investigated the effect of a rotor resistance parameter mismatch in the control algorithm on the angular rotor flux misalignment and the subsequent deviation of stator currents and motor torque from their setpoints. Hence, an online, data-driven torque compensation to eliminate the temperature effect is proposed to enable robust torque-controlled IMs. A model-based analysis and experimental mapping of the temperature effect on motor torque is presented. A temperature-torque lookup-table is subsequently implemented within the control algorithm demonstrating the ability to reduce the detrimental effect of temperature on torque control. Experimental results on a 5.5 kW squirrel-cage induction motor show that the proposed data-driven online temperature compensation method is able to reduce torque mismatch when compared to having no temperature compensation. Up to 17% torque mismatch is reduced at nominal torque and even up to 23% at torque setpoints that are lower than 20% of the nominal torque. A limited torque error of <1% remains in a broad operating range.

1 Introduction

Induction machines (IMs) are widely used in industry because of their simple and vigorous mechanical construction, low maintenance costs and acceptable efficiency in energy conversion [1, 2]. Advancements in power electronic components and circuits have enabled and driven research to progress on having efficient control strategies for IMs. Field-oriented control (FOC) is the most commonly used strategy nowadays because it allows flux and motor torque to be decoupled and controlled independently [3, 4]. However, inverter-supplied induction motors give rise to higher losses compared to a simple sinusoidal supply [5], causing increased temperatures in the motor.

To achieve FOC, the angular position of the rotor flux vector needs to be accurately known and can be attained either directly or indirectly. In direct field-oriented control, or DFOC, the position of the rotor flux is determined from flux measurements, which are both error-prone and expensive. Poor low-speed performance is also an issue of DFOC [3, 4, 6]. For these reasons, indirect field-oriented control (IFOC) is commonly used: the angular position of the rotor flux vector is estimated by integrating the sum of the measured rotor speed and the slip speed. For this to work, the (fixed) motor parameters in the controller, such as the rotor resistance and the motor inductances, need to be precisely known. This can be difficult as the rotor and stator resistances change during operation due to temperature variation. The motor inductances also vary due to magnetic saturation. These two phenomena cause a discrepancy between the real and the estimated angular position of the rotor flux vector, which results in an erroneous internal estimation of the motor torque and flux. These wrong estimations cause a deviation between the torque and rotor flux from their respective setpoints. This is especially problematic when the motor is used in torque control mode or when high torque precision is necessary. Furthermore, in the case of equivalent circuit modelling of the IM, it has been proved in [7] that the correct compensation of temperature and saturation is necessary to achieve accurate modelling.

A considerable amount of research has been dedicated to identify these parameter changes more accurately to attain robust operation towards temperature variations in the IMs, as also reviewed in [8]. Many methods for parameter identification have been explored in the literature [4]: signal injection methods [9, 10], model reference adaptive system (MRAS) [6, 11–17] and observer-based methods including the extended Kalman filter (EKF) [18]. Signal injection methods rely on the output response of a system while a test signal is injected at the system input. For example, in [9], a DC current test signal is injected into the motor neutral point to measure the stator winding resistance. However, a small amount of braking torque is subsequently generated. Signal injection methods generally interfere with the internal operation of the machine by generating a torque ripple. In [19], the authors circumvent this problem by using on the one hand the inherent pulse width modulation (PWM) content resulting from the modulated supply voltage and on the other hand the measurement of the resulting current ripple to estimate the rotor temperature through changes in the absolute value of the input impedance at PWM frequencies. This method, however, is only accurate if the current ripple is high enough.

An MRAS uses two models: a reference model for which the output signal is independent of the parameter under consideration and a second adjustable model for which the same output is a function of the unknown parameter. An adaptive controller adjusts the parameter in the adjustable model until the difference between the output of both models converges to zero. Different schemes can be obtained based on the choice of the output quantity: torque-based, reactive-power based, voltage-based or current-based. A drawback of MRAS is the sensitivity with respect to the common parameters in both the reference and adjustable models [20]. In the torque-based MRAS in the work of [13] for instance, the reference model also depends on the stator resistance, which varies with increasing temperature and is not constant during motor operation. An identification scheme is described in [6], where the d-axis decoupled reference voltage is used to tune the rotor resistance.

They report a steady-state accuracy and convergence rate that are superior to the EKF. In [16], a multi-rate MRAS is used to estimate the rotor time constant and multi-rate EKF is used to estimate the online load torque.

The aforementioned methods aim to accurately estimate the rotor time constant. However, they do not take other modelling inaccuracies into account. A data-driven methodology using a lookup-table (LUT) would inherently resolve these inaccuracies: the considered LUT, which is temperature dependent, is used to generate a compensated torque setpoint T^*_{comp} based on the desired torque setpoint T^*. This T^*_{comp} is then directly fed to the motor controller instead of the original setpoint T^*. This way, not only the uncertainty of the rotor time constant due to temperature variations is taken into account, but also any other uncertainty present in the considered motor model. Furthermore, a LUT that maps the torque versus temperature has the ability to provide additional information and insight into the physical phenomena (e.g. magnetic saturation) at play, in contrast to the parameter estimation methods described in the previous paragraph.

A data-driven LUT-based method can be used in any industrial application where accurate torque control of induction motors is needed. It can be applied in general for having high performance motion control in drivetrains. It can also be applied in an industrial context where a qualitative process is required such as in a steel mill environment where steel sheet rolling requires accurate tension forces on the sheets [21] to have high quality of the rolled metal [22]. The proposed methodology is also applicable for the identification of an unknown load torque for different operating points without using an expensive torque transducer. The IFOC induction motor with a classical proportional integral (PI) speed control loop commands the torque control loop, so that the output of the speed PI commands the motor torque setpoint. The motor subsequently drives the load at different speeds and the corresponding speed PI output should then be a measure for the driven unknown load torque. The motor torque drift due to thermal effects can then be compensated using the proposed data-driven LUT strategy. In this way, an induction motor can be used as a virtual transducer for an unknown load torque, which is more cost-effective than a physical torque sensor.

In this paper, the effect of having a rotor resistance mismatch in the control algorithm on the angular rotor flux misalignment and the subsequent deviation of stator currents and motor torque from their setpoints are investigated both analytically and experimentally. Furthermore, a data-driven torque compensation approach is proposed to reduce the detrimental effect of temperature on torque control. This is done by implementing a temperature-torque LUT in the control algorithm, the use of which requires little computation time. This approach is fundamentally different from the methods described in the previous paragraphs: instead of updating and tuning the rotor resistance parameter, in this paper a data-driven approach based on torque measurements is chosen to compensate directly the torque setpoint signal for a certain temperature rise. The most considerable advantage of this approach is that any complex, hard-to-model physical phenomenon is inherently accounted for in the proposed data-driven LUT based methodology. The drawback is the need for extensive torque measurements and a load emulator (that is speed controlled) mechanically connected in back-to-back configuration to the test motor (that is torque controlled).

The generation of the LUT involves emulating different rotor temperature increases by adapting the rotor resistance parameter value in the test motor controller. Emulation of different temperature increases ensures faster and more efficient generation of the LUT than waiting for the motor to heat up to the right temperature and measure the corresponding torque. When using an industrial motor drive, having writing access to the rotor time constant or rotor resistance parameter is thus a prerequisite to build the LUT. Finally, two practically feasible methods are presented to generate the LUT, one of which requires the use of the standard embedded temperature sensors in the stator windings, while the other requires an additional contactless temperature sensor to measure the rotor temperature directly.

Section 2 describes the modelling details of the IM and the IFOC, while Section 3 presents the analysis of thermal influence on both stator currents and motor torque. Section 4 illustrates the proposed data-driven methodology to compensate for the temperature effect on torque control by using a LUT. Section 5 describes the experimental setup and the obtained experimental results for the validation of the torque model, the generation of the LUTs and their subsequent use in the torque control algorithm to compensate for the temperature effect. Finally, conclusions are drawn in Section 6.

2 Indirect field-oriented controller

2.1 Field-oriented control

FOC decomposes the stator current according to a synchronous dq-reference frame where the d-axis is aligned with the position of the rotor flux vector $\mathbf{\Psi}_{\text{r}}$. The stator current component along the d-axis i_{ds} and the q-axis i_{qs} are perpendicular to each other and can be used to control $\mathbf{\Psi}_{\text{r}}$ and the motor torque T_{em} independently. $\| \mathbf{\Psi}_{\text{r}} \|$ and i_{ds} are related through a linear first-order transfer function with time constant $\tau_{\text{r}} = L_{\text{r}}/R_{\text{r}}$ being the ratio of rotor inductance L_{r} and rotor resistance R_{r}. The motor torque is proportional to i_{qs} when the rotor flux is kept constant. In this reference frame, $\psi_{d\text{r}} = \| \mathbf{\Psi}_{\text{r}} \|$ and $\psi_{q\text{r}} = 0 = \text{d}\psi_{q\text{r}}/\text{d}t$. To effectively decouple the control of flux and torque, it is necessary to know exactly the angular position of the rotor flux vector $\alpha_{\mathbf{\Psi}_{\text{r}}}$ with respect to the stator reference. For IFOC, $\alpha_{\mathbf{\Psi}_{\text{r}}}$ is estimated based on the slip speed ω_{sl}.

In an induction motor, the mechanical rotational speed Ω_{r} and electrical rotor speed ω_{r} are related by the number of pole pairs N_{p}:

$$\omega_{\text{r}} = N_{\text{p}}\Omega_{\text{r}} \tag{1}$$

Note that in the presented model of the electromagnetic torque, we assume that the motor does not experience magnetic saturation, i.e. the stator and rotor fluxes behave linearly with respect to the stator and rotor currents.

2.2 Indirect field-oriented controller

Fig. 1 schematically presents the operation of the IFOC. Ψ^*_{r} is the rotor flux setpoint, T^* is the torque setpoint and S_{a}, S_{b} and S_{c} are the inverter switching commands.

During each subsequent time step, the measured three-phase stator currents are transformed to the dq-reference frame through the Clarke and Park transformations, using $\alpha_{\mathbf{\Psi}_{\text{r}}}$ estimated in the previous time step to align the d-axis with the rotor flux vector. The component of the stator current along the d-axis $\hat{i}_{ds}$ is then used to estimate the rotor flux in the present iteration through the following first-order transfer function (s denotes the complex variable of the Laplace transform):

$$\| \hat{\mathbf{\Psi}}_{\text{r}} \| = \frac{L_{\text{m}}}{1 + \tau_{\text{r}} s}\hat{i}_{ds} \tag{2}$$

where L_{m} is the mutual inductance. This rotor flux estimate is subsequently used in the calculation of three quantities: $\hat{\alpha}_{\mathbf{\Psi}_{\text{r}}}$ for the next iteration, the desired d-component and q-component of the stator current i^*_{ds} and i^*_{qs} for the present iteration. By integrating the rotor speed ω_{r} and the estimated slip speed $\hat{\omega}_{\text{sl}}$, $\hat{\alpha}_{\mathbf{\Psi}_{\text{r}}}$ and the position of the dq-reference frame in the next iteration can be estimated:

$$\hat{\omega}_{\text{sl}} = \frac{L_{\text{m}}\hat{i}_{qs}}{\tau_{\text{r}} \| \hat{\mathbf{\Psi}}_{\text{r}} \|} \tag{3}$$

$$\hat{\alpha}_{\mathbf{\Psi}_{\text{r}}} = \int (\omega_{\text{r}} + \hat{\omega}_{\text{sl}})\,\text{d}t \tag{4}$$

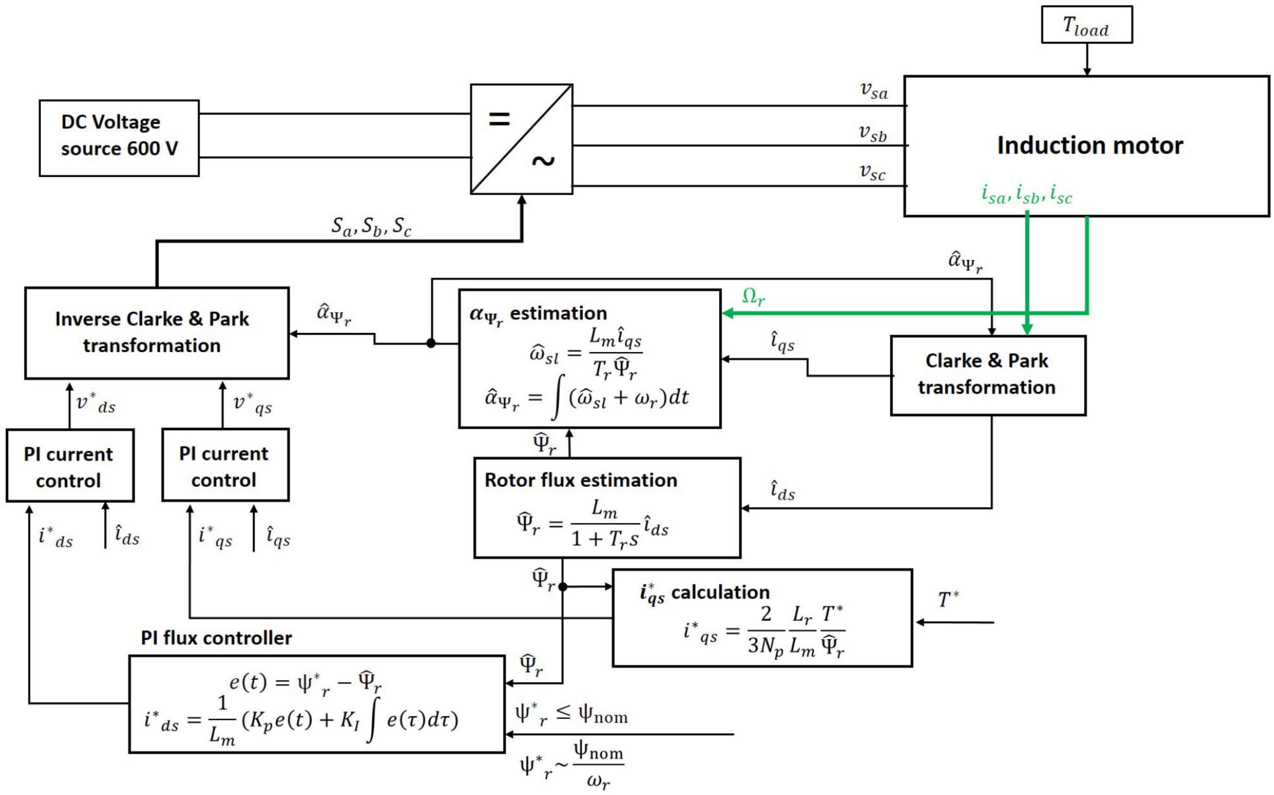
T_{load}
DC Voltage source 600 V
=
~
v_{sa}
v_{sb}
v_{sc}
Induction motor
i_{sa}, i_{sb}, i_{sc}
S_a, S_b, S_c
$\hat{\alpha}_{\Psi_r}$
Ω_r
Inverse Clarke & Park transformation
α_{Ψ_r} estimation
$\hat{\omega}_{sl} = \frac{L_m \hat{\imath}_{qs}}{T_r \hat{\Psi}_r}$
$\hat{\alpha}_{\Psi_r} = \int(\hat{\omega}_{sl} + \omega_r)dt$
$\hat{\imath}_{qs}$
Clarke & Park transformation
v^*_{ds}
v^*_{qs}
$\hat{\Psi}_r$
PI current control
PI current control
Rotor flux estimation
$\hat{\Psi}_r = \frac{L_m}{1 + T_r s}\hat{\imath}_{ds}$
$\hat{\imath}_{ds}$
i^*_{ds}
$\hat{\imath}_{ds}$
i^*_{qs}
$\hat{\imath}_{qs}$
i^*_{qs} calculation
$i^*_{qs} = \frac{2}{3N_p}\frac{L_r}{L_m}\frac{T^*}{\hat{\Psi}_r}$
T^*
PI flux controller
$e(t) = \psi^*_r - \hat{\Psi}_r$
$i^*_{ds} = \frac{1}{L_m}(K_p e(t) + K_I \int e(\tau)d\tau)$
$\psi^*_r \leq \psi_{\text{nom}}$
$\psi^*_r \sim \frac{\psi_{\text{nom}}}{\omega_r}$

Fig. 1 *Schematic representation of the operation of an IFOC. The hat sign (^) denotes quantities that are estimated by the IFOC, while the star superscript (*) denotes setpoints.* v_{sa}, v_{sb} *and* v_{sc} *are the three-phase stator voltages;* v_{ds} *and* v_{qs} *the decomposed dq stator voltages;* T_{load} *the load torque applied to the motor shaft; T the motor torque;* i_{sa}, i_{sb} *and* i_{sc} *the three-phase stator currents;* i^*_{ds} *and* i^*_{qs} *the decomposed dq stator currents;* Ω_r *the mechanical rotor speed;* ω_r *the electrical rotor speed;* $\boldsymbol{\Psi}_r$ *the rotor flux, which never exceeds the nominal rotor flux* $\boldsymbol{\Psi}_{\text{nom}}$*;* $\alpha_{\boldsymbol{\Psi}_r}$ *is the angle between the rotor flux vector and the stator reference and* S_a, S_b *and* S_c *are the switching commands to the inverters*

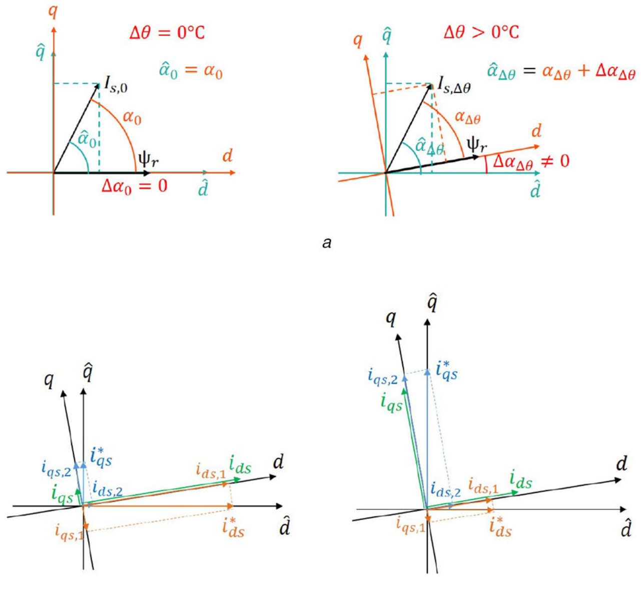
q
$\hat{q}$
$\Delta\theta = 0°C$
$\hat{\alpha}_0 = \alpha_0$
$I_{s,0}$
α_0
$\hat{\alpha}_0$
ψ_r
d
$\Delta\alpha_0 = 0$
$\hat{d}$
q
$\hat{q}$
$\Delta\theta > 0°C$
$\hat{\alpha}_{\Delta\theta} = \alpha_{\Delta\theta} + \Delta\alpha_{\Delta\theta}$
$I_{s,\Delta\theta}$
$\alpha_{\Delta\theta}$
$\hat{\alpha}_{\Delta\theta}$
ψ_r
d
$\Delta\alpha_{\Delta\theta} \neq 0$
$\hat{d}$
q
$\hat{q}$
$i_{qs,2}$
i^*_{qs}
i_{qs}
$i_{ds,2}$
$i_{ds,1}$
i_{ds}
d
$i_{qs,1}$
i^*_{ds}
$\hat{d}$
q
$\hat{q}$
$i_{qs,2}$
i^*_{qs}
i_{qs}
$i_{ds,2}$
$i_{ds,1}$
i_{ds}
d
$i_{qs,1}$
i^*_{ds}
$\hat{d}$

a

b

Fig. 2 *Effect of temperature on the accuracy of the calculated dq-frame angular position and on the stator current components*

(a) A rise in rotor temperature $\Delta\theta$ causes a linear rise of the rotor resistance, which results both in an inaccurate rotor flux angle and a phase shift $\Delta\alpha_{\Delta\theta}$ between the calculated and actual angular position of the *dq*-frame, ***(b)*** Left: Misalignment of the *dq*-reference frame for low stator current phasor angles. Right: Misalignment of *dq*-reference frame for high stator current phasor angles

Notice that the calculation of both the magnitude of $\hat{\boldsymbol{\Psi}}_r$ and its angle $\hat{\alpha}_{\boldsymbol{\Psi}_r}$ depend directly on R_r through the time constant τ_r.

3 Analysis of temperature effect on stator currents and motor torque

The IFOC considered in this paper uses a number of constant parameters in the estimation of magnetic and electrical quantities. These include the rotor resistance R_r, the rotor inductance L_r and the mutual inductance L_m. As such, the considered IFOC operates assuming that those three parameters stay fixed: it supposes that there is no temperature increase present affecting the rotor resistance, and that there is no magnetic saturation during operation potentially reducing mutual and rotor inductance values. All of these effects actually do occur during operation and ideally need to be taken into account accordingly. The results of [23] show that the calculated torque T_{em} is most sensitive to variation in R_r, followed by L_m and finally L_r.

The temperature-dependent electrical resistance $R_r(\theta)$ considered in this paper varies according to:

$$R_r(\theta) = R_{r0}(1 + a_{\text{Al}}(\theta - 22°\text{C})) \tag{5}$$

with R_{r0} is the rotor resistance at 22°C and $a_{\text{Al}} = 0.0043/°\text{C}$ is the temperature coefficient of resistance of aluminium. Skin effect in the rotor cage is neglected in this work as the slip frequency at full load does not exceed 5 Hz.

As R_r increases during motor operation due to rising temperature, the estimated rotor flux angle $\hat{\alpha}_{\boldsymbol{\Psi}_r}$ according to (4) deflects from reality. Consequently, the angular position of the *dq*-reference frame has a deviation $\Delta\alpha_{\Delta\theta}$ with the actual *dq*-reference frame. This has been reported in various studies such as [6, 13, 20, 24]. Fig. 2*a* illustrates the effect of $\Delta\theta$ on the *dq*-reference frame.

3.1 Effect of temperature on stator currents

Due to the deviation angle $\Delta\alpha_{\Delta\theta}$, the decomposition of the stator current vector $\boldsymbol{I}_{s,\Delta\theta}$ according to the IFOC *dq*-frame no longer results in decoupled commands for torque and rotor flux. This means that the current commands i_{ds}^* and i_{qs}^* do not translate anymore into perpendicular current components related to the actual angular position of $\boldsymbol{\Psi}_\mathrm{r}$, so that $i_{ds} \neq i_{ds}^*$ and $i_{qs} \neq i_{qs}^*$, as shown in Fig. 2*b*. This in turn results in an increase of rotor flux magnitude and a positive or negative deviation of motor torque depending on its setpoint.

From Fig. 2*b* the *dq* components of stator current can be written as follows:

$$i_{qs} = i_{qs,2} - i_{qs,1} \tag{6}$$

$$i_{ds} = i_{ds,1} + i_{ds,2} \tag{7}$$

It can also be seen that the current components can be related to $\Delta\alpha_{\Delta\theta}$:

$$\begin{cases} i_{qs,1} = i_{ds}^* \sin(\Delta\alpha_{\Delta\theta}) \\ i_{ds,1} = i_{ds}^* \cos(\Delta\alpha_{\Delta\theta}) \\ i_{qs,2} = i_{qs}^* \cos(\Delta\alpha_{\Delta\theta}) \\ i_{ds,2} = i_{qs}^* \sin(\Delta\alpha_{\Delta\theta}) \end{cases} \tag{8}$$

The stator currents can then be rewritten as:

$$\begin{cases} i_{qs} = i_{qs}^* \cos(\Delta\alpha_{\Delta\theta}) - i_{ds}^* \sin(\Delta\alpha_{\Delta\theta}) \\ i_{ds} = i_{ds}^* \cos(\Delta\alpha_{\Delta\theta}) + i_{qs}^* \sin(\Delta\alpha_{\Delta\theta}) \end{cases} \tag{9}$$

From the substitution of (9) in the equation below, it follows that the magnitude of the stator current vector $\boldsymbol{I}_{\mathrm{s},\Delta\theta}$ does not change under a temperature increase [24]:

$$\| \boldsymbol{I}_{\mathrm{s},\Delta\theta} \| = \sqrt{i_{ds}^2 + i_{qs}^2} \overset{(9)}{=} \sqrt{(i_{ds}^*)^2 + (i_{qs}^*)^2} = \| \boldsymbol{I}_{\mathrm{s},0} \| = \| \boldsymbol{I}_\mathrm{s} \| \tag{10}$$

The current components i_{ds}, i_{qs}, i_{ds}^* and i_{qs}^* are also related to the current magnitude $\| \boldsymbol{I}_\mathrm{s} \|$ according to the following expressions:

$$\begin{cases} i_{ds} = \| \boldsymbol{I}_\mathrm{s} \| \cos(\alpha_{\Delta\theta}) \\ i_{qs} = \| \boldsymbol{I}_\mathrm{s} \| \sin(\alpha_{\Delta\theta}) \\ i_{ds}^* = \| \boldsymbol{I}_\mathrm{s} \| \cos(\alpha_0) \\ i_{qs}^* = \| \boldsymbol{I}_\mathrm{s} \| \sin(\alpha_0) \end{cases} \tag{11}$$

with α_0 and $\alpha_{\Delta\theta}$ being the angle of the stator current vector with respect to the actual rotor flux vector without and with a non-zero temperature increase $\Delta\theta$, respectively. Finally, the actual and estimated angles α and $\hat{\alpha}$ of the stator current vector are related as shown in Fig. 2*a*:

$$\hat{\alpha}_{\Delta\theta} = \hat{\alpha}_0 = \alpha_0 \tag{12}$$

$$\alpha_{\Delta\theta} = \alpha_0 - \Delta\alpha_{\Delta\theta} \tag{13}$$

3.2 Effect of temperature on motor torque

In this subsection, an expression that relates the relative motor torque deviation $\Delta T / T^*$ to the temperature effect (change of temperature $\Delta\theta$ in the rotor) at a certain setpoint T^* is determined:

$$\frac{\Delta T}{T^*} = g(\Delta\theta, T^*) \tag{14}$$

The function g in (14) depends on a number of physical motor parameters.

The IM electromagnetic torque in the case of steady-state conditions and no magnetic saturation phenomena is

$$T_\mathrm{em} = \frac{3}{2} N_\mathrm{p} \frac{L_\mathrm{m}}{L_\mathrm{r}} \| \boldsymbol{\Psi}_\mathrm{r} \| \, i_{qs} = \frac{3}{2} N_\mathrm{p} \frac{L_\mathrm{m}^2}{L_\mathrm{r}} i_{ds} i_{qs} \tag{15}$$

The motor torque at room temperature $T_{\mathrm{em},0}$ and at elevated temperature $T_{\mathrm{em},\Delta\theta}$ can be written as

$$T_{\mathrm{em},0} = k i_{ds}^* i_{qs}^* \tag{16}$$

$$T_{\mathrm{em},\Delta\theta} = k i_{ds} i_{qs} \tag{17}$$

respectively with $k = (3/2) N_\mathrm{p} (L_\mathrm{m}^2 / L_\mathrm{r})$. The relative motor torque deviation $\Delta T = T_{\mathrm{em},\Delta\theta} - T_{\mathrm{em},0}$ can subsequently be expressed as a function of the *dq* stator components:

$$\frac{\Delta T}{T_{\mathrm{em},0}} = \left(\frac{T_{\mathrm{em},\Delta\theta}}{T_{\mathrm{em},0}} - 1 \right) = \left(\frac{i_{ds}}{i_{ds}^*} \frac{i_{qs}}{i_{qs}^*} - 1 \right) \tag{18}$$

Substitution of (11) in (18) results in

$$\frac{\Delta T}{T_{\mathrm{em},0}} = \left(\frac{\| \boldsymbol{I}_\mathrm{s} \| \cos(\alpha_{\Delta\theta})}{\| \boldsymbol{I}_\mathrm{s} \| \cos(\alpha_0)} \frac{\| \boldsymbol{I}_\mathrm{s} \| \sin(\alpha_{\Delta\theta})}{\| \boldsymbol{I}_\mathrm{s} \| \sin(\alpha_0)} - 1 \right) \tag{19}$$

$$\frac{\Delta T}{T_{\mathrm{em},0}} = \left(\frac{\sin(2\alpha_{\Delta\theta})}{\sin(2\alpha_0)} - 1 \right) \tag{20}$$

Substitution of (13) in the expression above and stating that $T_{\mathrm{em},0}$ equals the torque setpoint T^* gives the following result:

$$\frac{\Delta T}{T^*} = \left(\frac{\sin(2(\alpha_0 - \Delta\alpha_{\Delta\theta}))}{\sin(2\alpha_0)} - 1 \right) \tag{21}$$

To arrive at an expression for torque deviation of the form (14), both α_0 and $\Delta\alpha_{\Delta\theta}$ need to be rewritten as explicit functions of T^*, $\Delta\theta$ and other motor parameters. First, α_0 can be related to the ratio of i_{qs}^* and i_{ds}^* through the tangent of α_0 [24], as seen in Fig. 2*a*. Let us define

$$f \equiv \frac{i_{qs}^*}{i_{ds}^*} = \tan(\alpha_0) \tag{22}$$

Under steady-state conditions the *dq* current commands can be rewritten as:

$$i_{ds}^* = \frac{\Psi_\mathrm{r}^*}{L_\mathrm{m}} \quad i_{qs}^* = \frac{2 L_\mathrm{r} T^*}{3 N_\mathrm{p} L_\mathrm{m} \Psi_\mathrm{r}^*} \tag{23}$$

Combining (22) and (23) finally results in an explicit expression for α_0:

$$\alpha_0 = \mathrm{atan}(f) = \mathrm{atan}\left(\frac{i_{qs}^*}{i_{ds}^*} \right) = \mathrm{atan}\left(\frac{2 L_\mathrm{r} T^*}{3 N_\mathrm{p} (\Psi_\mathrm{r}^*)^2} \right) \tag{24}$$

Second, to arrive at an explicit solution for $\Delta\alpha_{\Delta\theta}$, it is necessary to look at the slip speed. Under steady-state conditions, the estimated slip speed equals the actual slip speed [24, 25]:

$$\hat{\omega}_{\mathrm{sl},\infty} = \omega_{\mathrm{sl},\infty} \tag{25}$$

Combining (3) and (23) results in the following expression:

$$\frac{i_{qs}^*}{\hat{\tau}_\mathrm{r} i_{ds}^*} = \frac{i_{qs}}{\tau_\mathrm{r} i_{ds}} \tag{26}$$

Subsequent substitution of (9) results in:

$$\frac{i_{qs}^*}{\hat{\tau}_\mathrm{r} i_{ds}^*} = \frac{i_{qs}^* \cos(\Delta\alpha_{\Delta\theta}) - i_{ds}^* \sin(\Delta\alpha_{\Delta\theta})}{\tau_\mathrm{r} (i_{ds}^* \cos(\Delta\alpha_{\Delta\theta}) + i_{qs}^* \sin(\Delta\alpha_{\Delta\theta}))} \tag{27}$$

Rewriting (27) for $\tan(\Delta\alpha_{\Delta\theta})$:

$$\tan(\Delta\alpha_{\Delta\theta}) = \frac{i_{ds}^{*} i_{qs}^{*} (\hat{\tau}_{\mathrm{r}} - \tau_{\mathrm{r}})}{\hat{\tau}_{\mathrm{r}} (i_{ds}^{*})^{2} + \tau_{\mathrm{r}} (i_{qs}^{*})^{2}} \tag{28}$$

The estimated and real rotor time constant are written as:

$$\hat{\tau}_{\mathrm{r}} = \frac{L_{\mathrm{r}}}{R_{\mathrm{r}0}}, \quad \tau_{\mathrm{r}} = \frac{L_{\mathrm{r}}}{R_{\mathrm{r}0} + \Delta R_{\mathrm{r}}} \tag{29}$$

where ΔR_{r} is the rotor resistance mismatch due to a rotor temperature increase $\Delta\theta$. Equation (28) then becomes:

$$\tan(\Delta\alpha_{\Delta\theta}) = \frac{\Delta R_{\mathrm{r}}}{(R_{\mathrm{r}0} + \Delta R_{\mathrm{r}})(i_{ds}^{*}/i_{qs}^{*}) + R_{\mathrm{r}0}(i_{qs}^{*}/i_{ds}^{*})} \tag{30}$$

After rewriting (30) and remembering the definition of f according to (22), the misalignment angle $\Delta\alpha_{\Delta\theta}$ can be expressed as a function of f and ΔR_{r}:

$$\Delta\alpha_{\Delta\theta} = \operatorname{atan}\left(\frac{f \Delta R_{\mathrm{r}}}{R_{\mathrm{r}0}(f^{2} + 1) + \Delta R_{\mathrm{r}}}\right) \tag{31}$$

If the rotor resistance varies linearly (with proportionality constant a_{Al}) with temperature, then $\Delta R_{\mathrm{r}} = R_{\mathrm{r}} - R_{\mathrm{r}0} = R_{\mathrm{r}0} a_{\mathrm{Al}} \Delta\theta$ and $\Delta\alpha_{\Delta\theta}$ can finally be written as an explicit function of $\Delta\theta$, T^{*} (through f) and other motor parameters:

$$\Delta\alpha_{\Delta\theta} = \operatorname{atan}\left(\frac{f a_{\mathrm{Al}} \Delta\theta}{(f^{2} + 1) + a_{\mathrm{Al}} \Delta\theta}\right) \tag{32}$$

Substitution of (24) and (32) in (21) finally yields the analytical expression for the relative deviation of torque as an explicit function of $\Delta\theta$, T^{*} and other motor parameters. Expression (14) is now the following explicit function:

$$\frac{\Delta T}{T^{*}} = \frac{\sin(2\operatorname{atan}(f/(1 + a_{\mathrm{Al}}\Delta\theta)))}{\sin(2\operatorname{atan}(f))} - 1 \tag{33}$$

with

$$f = \frac{2 L_{\mathrm{r}} T^{*}}{3 N_{\mathrm{p}} (\Psi_{\mathrm{r}}^{*})^{2}} \tag{34}$$

Equation (33) can be further simplified by keeping in mind that $\sin(2\operatorname{atan}(x)) = 2x/(1 + x^{2})$. This results in the following simplified expression for the relative torque deviation:

$$\frac{\Delta T}{T^{*}} = \frac{(1 + a_{\mathrm{Al}}\Delta\theta)(1 + f^{2})}{(1 + a_{\mathrm{Al}}\Delta\theta)^{2} + f^{2}} - 1 \tag{35}$$

This simplified result for torque deviation confirms the findings presented in [24] for the resulting torque due to a mismatch in rotor time constant τ_{r}. Using (21) and (24), the relative deviation of the motor torque can be visualised as a function of T^{*} and this for different $\Delta\alpha_{\Delta\theta}$ values. Fig. 3*a* shows that a larger $\Delta\alpha_{\Delta\theta}$ leads to a larger torque deviation for the same torque setpoint T^{*}, but the sign and magnitude of this deviation also depends on T^{*} itself: there are tipping points for which ΔT is zero, even for large $\Delta\alpha_{\Delta\theta}$.

Fig. 3*b* illustrates $\Delta\alpha_{\Delta\theta}$ as a function of T^{*} and $\Delta\theta$. The relation between $\Delta\alpha_{\Delta\theta}$ and $\Delta\theta$ is quasi-linear. However, the slope of this function is also dependent on T^{*}, as illustrated in the figure. This trend also qualitatively aligns with the work presented in [26]. For T^{*} up to 40% of T_{nom}, the slope of the $\Delta\alpha_{\Delta\theta}$ curves as a function of $\Delta\theta$ increases with T^{*}. If T^{*} increases further, the slope slowly decreases again.

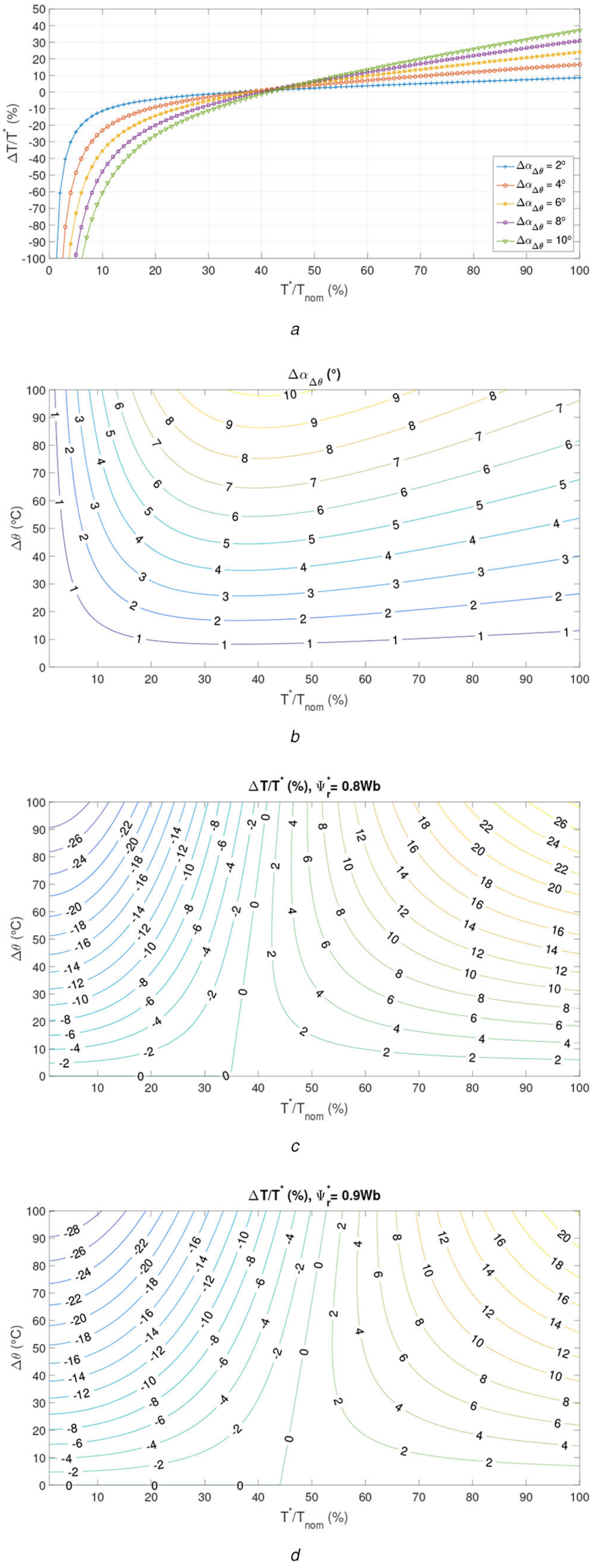

Fig. 3 *Effect of temperature on the misalignment angle and on motor torque*

(a) Relative deviation of the motor torque (in %) as a function of the torque setpoint T^{*} for different values of $\Delta\alpha_{\Delta\theta}$. Calculations are based on the specifications of the considered IM, cf. Table 1. The nominal torque is $T_{\mathrm{nom}} = 35.97$ Nm, ***(b)*** Angular misalignment $\Delta\alpha_{\Delta\theta}$ (in °) as a function of $\Delta\theta$ and T^{*} according to (32), ***(c)***, ***(d)*** Relative deviation of motor torque (in %) as a function of T^{*} and $\Delta\theta$ according to (33). $\Psi_{\mathrm{r}}^{*} = 0.8$ Wb and $\Psi_{\mathrm{r}}^{*} = 0.9$ Wb respectively

Table 1 Induction motor specifications

Characteristic	Symbol	Value	Units
number of pole pairs	N_p	2	—
nominal power	P_N	5.5	kW
nominal speed	$\Omega_{\mathrm{r,N}}$	1460	rpm
nominal torque	T_nom	35.97	Nm
nominal current	I_N	18.6/10.7 Δ/Y	A
nominal voltage	U_N	230/400 Δ/Y	V
efficiency	η	89.6	%
mutual inductance	L_m	146.7	mH
stator inductance	L_s	153	mH
rotor inductance	L_r	153.3	mH
stator resistance at 22°C	R_s	0.625	Ω
rotor resistance at 22°C	R_r	0.469	Ω

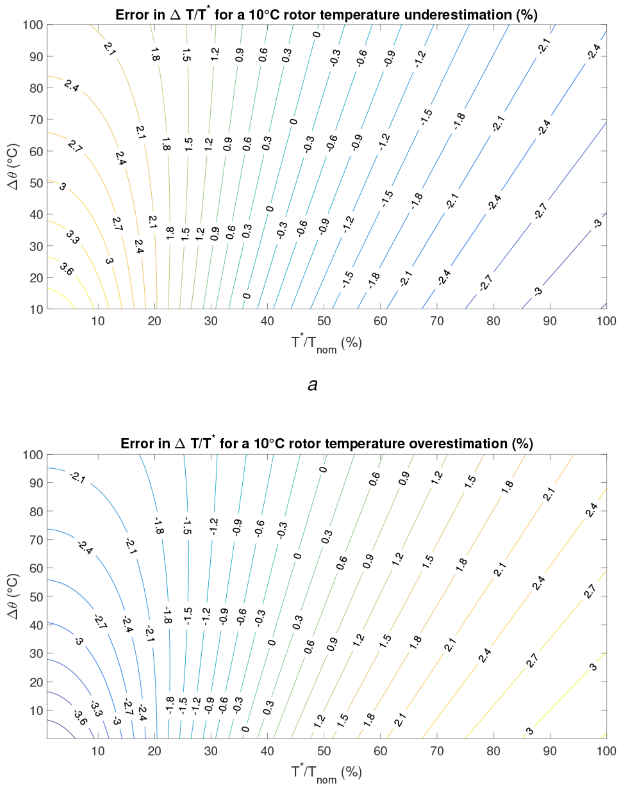

a

b

Fig. 4 *Sensitivity analysis: deviation from the torque mapping (in %) presented in Fig. 3c*

(a) For a 10°C underestimation of the rotor temperature, ***(b)*** For a 10°C overestimation of the rotor temperature

Fig. 3*c* illustrates the torque deviation as a function of T^* and $\Delta\theta$ according to (35) for $\Psi_\mathrm{r}^* = 0.8$ Wb and the motor characteristics listed in Table 1. For example, at a torque setpoint of 15% nominal torque T_nom, an increase in temperature means a decrease in motor torque, whereas for a torque setpoint at 85% of T_nom, a temperature increase causes an increase in motor torque. These trends have also been shown in earlier studies [13, 24, 27]. The tipping points for which $\Delta T = 0$ in Fig. 3*a* are visible in Fig. 3*c* as a zero-line. This line depends on the motor characteristics (N_p, L_r and a_Al), the rotor flux setpoint Ψ_r^* and $\Delta\theta$, and can be determined analytically by demanding $\Delta T = 0$ in (35) with f determined according to (34):

$$\frac{\Delta T}{T^*} = \frac{(1 + a_\mathrm{Al}\Delta\theta)(1 + f^2)}{(1 + a_\mathrm{Al}\Delta\theta)^2 + f^2} - 1 = 0 \tag{36}$$

Further simplification of (36) and using (34) gives

$$1 + f^2 = 2 + a_\mathrm{Al}\Delta\theta \tag{37}$$

$$\left(\frac{2L_\mathrm{r}T^*}{3N_\mathrm{p}(\Psi_\mathrm{r}^*)^2}\right)^2 = 1 + a_\mathrm{Al}\Delta\theta \tag{38}$$

The zero-line is finally written as

$$T^*(\Delta T = 0) = \sqrt{1 + a_\mathrm{Al}\Delta\theta}\,\frac{3N_\mathrm{p}}{2L_\mathrm{r}}(\Psi_\mathrm{r}^*)^2 \tag{39}$$

First, (39) confirms that the tipping points $T^*(\Delta T = 0)$ on the zero-line increase for increasing values of $\Delta\theta$, as shown in Fig. 3*c*. Second, it is also clear that the zero-line shifts to higher T^* for higher Ψ_r^* and to lower T^* for lower Ψ_r^*. Fig. 3*d* illustrates the influence of having a higher rotor flux ($\Psi_\mathrm{r}^* = 0.9$ Wb) setpoint. This indeed shifts the zero-line to higher T^* and negatively increases the torque deviation at lower torques, while a lower Ψ_r^* shifts the zero-line to lower T^* and increases the torque deviation at higher torques. The values illustrated in Figs. 3*c* and *d* assume motor operation in the linear magnetic region.

3.3 Sensitivity of torque mapping with respect to the accuracy of rotor temperature

As it is difficult to practically measure the temperature of the rotor bars, it is useful to investigate the effect of a rotor temperature measurement fault on the torque mapping presented in the previous subsection (cf. Fig. 3*c*). The error in predicted torque deviation as a result of a 10°C underestimation and overestimation of the rotor temperature is illustrated in Figs. 4*a* and *b*, respectively. These figures are obtained by vertically shifting Fig. 3*c* by 10°C up for a rotor temperature overestimation and 10°C down for an underestimation, and then subtract the original values of Fig. 3*c* from the shifted values. For both cases, relative errors are higher in absolute value for smaller $\Delta\theta$ and also become higher further away from the zero-line, ranging from 0 to 3.8%. In the case of a rotor temperature underestimation, the predicted $|\Delta T|$ is underestimated for the entire range of T^*, while for a temperature overestimation $|\Delta T|$ is overestimated for all T^*. This analysis shows that while a rotor temperature measurement error lower than 10°C will not result in dramatic errors, a higher accuracy in rotor temperature measurement still means an accuracy increase in the prediction of torque deviation.

4 Data-driven methodology to compensate for the temperature effect on torque control using a LUT

As discussed in the Introduction, a data-driven method using a LUT to compensate for the detrimental effect of temperature on torque control is proposed and implemented on an experimental setup. This methodology is illustrated in Figs. 5*a* and *b*.

Next to the torque setpoint T^* that is input to the methodology we also need to provide information on the rotor temperature $\Delta\theta$. This can be deduced from direct measurements, e.g. the infrared (IR) sensor considered in this paper, from thermal modelling, or from indirect measurements that employ e.g. Kalman-type filtering. The latter two are here considered as being out of the scope of this paper.

Both T^* and $\Delta\theta$ are fed to the LUT, which then yield the compensated torque setpoint $T_\mathrm{comp}^* = T^* - \Delta T(T_\mathrm{comp}^*, \Delta\theta)$. The latter is subsequently supplied to the IFOC controller. For example, if $T^* = 30$ Nm and $\Delta\theta = 60$°C the LUT will output a compensated torque setpoint of $T_\mathrm{comp}^* = 27.13$ Nm, as indicated by the dashed arrows in Fig. 5*b*. Notice that for a certain $\Delta\theta$, T_comp^* as a function of T^* is monotonically increasing, which ensures a one-on-one relation between T^* and T_comp^*. This ensures a unique solution for every T^*. The advantage of this data-driven methodology is that any discrepancy that has an effect on the torque-temperature relation, between the motor model on the one hand and the

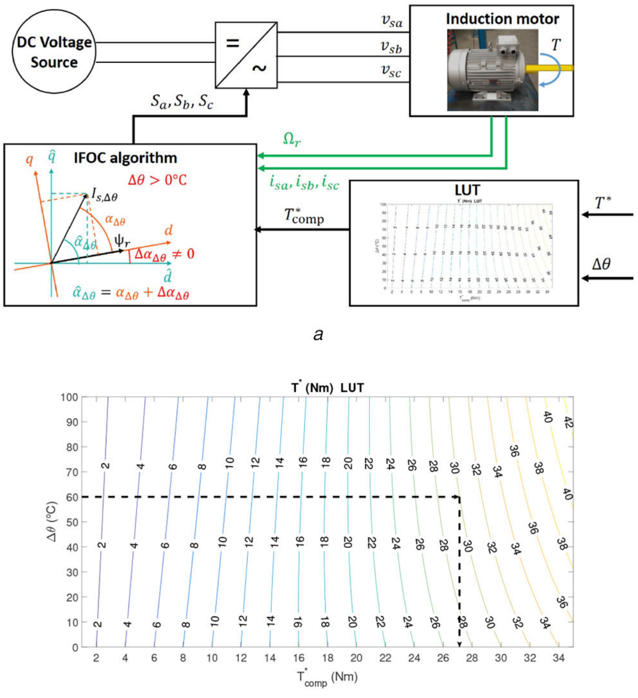

b

Fig. 5 *Data-driven LUT-based temperature compensation for torque*
(a) Schematic representation of the integration of a data driven LUT-based temperature compensation for torque in the controller, ***(b)*** Example of the LUT used for the compensation of the temperature effect on torque control. For a certain rotor temperature increase $\Delta\theta$ the compensated torque setpoint T^*_{comp} corresponding to the desired T^* is found. For example, when $\Delta\theta = 60$°C and $T^* = 30$ Nm, the LUT outputs $T^*_{\mathrm{comp}} = 27.13$ Nm, as indicated by the dashed arrows. This LUT is based on the motor parameters listed in Table 1 and fine tuned as discussed in Section 5.3

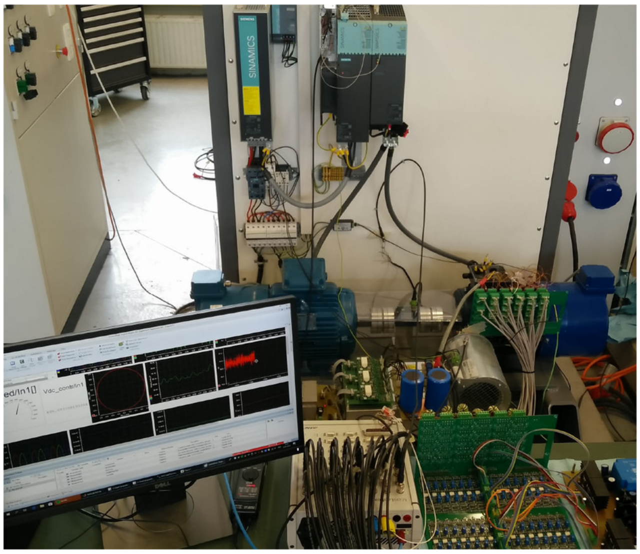

Fig. 6 *Picture of the experimental test setup. A 5.5 kW test motor (right) is mechanically coupled to a 7.5 kW (left) load emulator. The real-time interface of the dSPACE MicroLabBox is used both for motor control and data acquisition*

physical motor entity itself on the other hand, is already inherently being accounted for in the LUT.

The LUT can be generated in two ways: either on an analytical basis or on an experimental basis. Measurements will be necessary in both cases: the analytical torque model as discussed in the previous section needs to be tuned for every considered motor, whereas a full torque measurement campaign needs to be performed for the data-driven approach. The advantages of the analytical approach are on the one hand the insight and information gained in the physical system and on the other hand the limited amount of torque measurements necessary to tune the torque model. However, the analytical model can still be error-prone, a problem which can be alleviated by adopting a full data-driven methodology (without underlying physical relations) and performing an extensive torque measurement campaign. As the latter method can accommodate for modelling inaccuracies (e.g. magnetic saturation) we generate in this paper the LUT on that basis. The disadvantage, however, is the necessity to generate a rather time-consuming data mapping.

The following section describes the experimental setup, the generation of the LUT using two practical methods, the experimental tuning and the validation of the analytical torque model as described in the previous section. Finally, the data-driven LUT is implemented in the test motor controller with the presentation and discussion of performance results.

5 Experimental results, validation and discussion

5.1 Experimental setup

An experimental setup is built to validate the analytical temperature-torque model developed in the previous section and to test the proposed online data-driven torque compensation with respect to temperature within the induction motor control. The induction motor under consideration is a squirrel-cage, 4 pole 5.5 kW motor, with a nominal speed of 1460 rpm. Its most important quantities with their corresponding values extracted at room temperature (22°C) are listed in Table 1.

The experimental setup (Fig. 6) consists of this test motor, mechanically connected to the load emulator (a 7.5 kW induction motor). The test motor is controlled with an in-house implementation of IFOC while the load emulator is controlled with V/f control using the Sinamics S120 Modular Drive System, which is an industrial motor drive. A 600 V DC source is connected to the 5.5 kW test motor via an inverter whose switches are commanded by the IFOC control algorithm programmed in the real-time interface of the dSPACE MicroLabBox system. The switching frequency of the three-phase inverter is 8 kHz. The IFOC control algorithm has been built in the Matlab Simulink environment (Matlab 2015b), and is subsequently uploaded in the RTI of the MicroLabBox.

Data acquisition of all sensor signals is also processed simultaneously through the MicroLabBox. A Lorenz Messtechnik GmbH, type DR-2112 torque sensor of 50 Nm rating and with an accuracy of ±0.05 Nm is connected between the two motors through single-lamellar couplings. A standard 1024 incremental encoder (BEI Sensors, type DHO5) is mounted on the shaft of the load emulator to measure rotor speed. Three Hall-effect LEM current transducers are employed to measure the three-phase stator currents of the 5.5 kW test motor. PT1000 contact temperature sensors class A have been embedded into the stator windings, stator laminations (for which small holes have been drilled) and frame of the test motor to monitor the temperature. A dedicated in-house designed board has been developed to obtain reliable temperature measurements capable of withstanding the EMI caused by the high voltage inverter switching frequency (noise amplitude smaller than 0.5°C). A contactless IR thermal sensor of type MLX90614-ACC has been additionally mounted through a small hole in the endcap and positioned close to the rotor so that its field of view is completely directed upon the rotor surface at the drive side end. The accuracy of the IR-sensor ranges from ±0.5 to ±1°C.

The test motor, load emulator and inverter boards are cooled with independent cooling ventilators. Commanding torque, flux and speed setpoints on the one hand and data-acquisition of sensor signals on the other hand are performed with dSPACE ControlDesk 6.1 software.

During operation, the 5.5 kW test motor is torque-controlled with IFOC, while the load emulator is speed-controlled in V/f. The inverter boards supplying the 5.5 kW test motor are not designed for generator operation, which means that the load emulator needs to operate in oversynchronous mode. This can be done by driving the torque of the test motor in the same orientation as the speed orientation of the load emulator. This way, energy is transferred

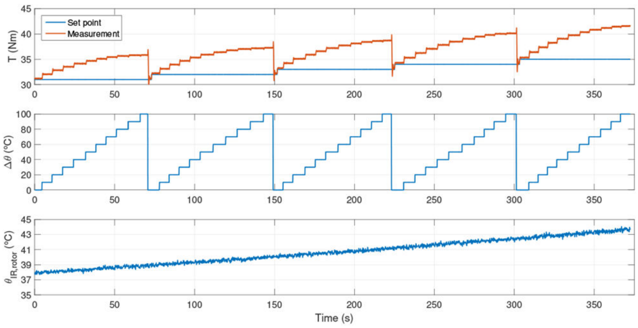

Fig. 7 *Measurements of torque T, emulated rotor temperature increase* $\Delta\theta$ *and measured physical rotor temperature* $\theta_{\mathrm{IR,rotor}}(t)$ *during one set of type-II measurements.* T^* *in this figure varies from 31 to 35 Nm in steps of 1 Nm, where for each step the artificial rotor temperature is varied from 0 to 100°C in steps of 10°C*

only from the test motor to the load emulator, which is then injected back into the grid.

5.2 Generation of the LUT by performing a torque measurement campaign

In this subsection two methods are presented to generate the data-driven LUT efficiently by performing a torque measurement campaign where the rotor temperature increase is emulated.

The initial motor parameters R_s, R_r, L_r and L_s in Table 1 are determined in the cold state at 22°C through a state-of-the-art method. During the generation of each point of the LUT using either of the two methods, the 7.5 kW load emulator is given a low-speed setpoint of $\Omega_r = 300\,\mathrm{rpm}$, while the 5.5 kW test motor is given a varying torque setpoint T^* and a constant rotor flux setpoint of $\Psi_r^* = 0.8\,\mathrm{Wb}$. The effect of an R_r mismatch between the controller and the physical system is emulated by manipulating the parameter in the controller such that an equivalent desired error is achieved. In other words, to emulate a certain increase in rotor resistance ΔR_r due to a temperature increase $\Delta\theta$ in the rotor, the initially calculated value of R_{r0} at room temperature (22°C) in Table 1 that is used in the controller, is now replaced by:

$$R_{\mathrm{r,emul}} = \frac{R_{\mathrm{r0}}}{1 + a_{\mathrm{Al}}\Delta\theta} \tag{40}$$

Emulating a desired rotor temperature increase $\Delta\theta$ by changing $\Delta\theta$ manually is much more time-efficient as it alleviates the problem of waiting for the motor to heat up to the right temperature, and circumvents the difficult measurement of the rotor resistance. To have full control over the temperature emulation, the actual temperature of the rotor should ideally remain constant during the generation of the LUT, which is impossible if the motor is operating at a non-zero torque and speed. Two ways are proposed to solve this conundrum.

The first is to keep the actual rotor temperature as close as possible to room temperature (22°C), to which end the complete set of measurements is divided into smaller sets with intermittent cooldown cycles and is designed so that the motor temperature never exceeds 30°C. This means that in the temperature emulation tests, a maximal error of 8°C can occur. Referring to Figs. 4*a* and *b* this translates roughly into a maximal error in $\Delta T/T^*$ of not >3%, although it is much lower in a large area of operation.

The second method is to compensate for the actual rotor temperature increase by using the contactless IR-sensor mounted inside the motor at the drive side end to measure the rotor temperature. The rotor resistance parameter $R_{\mathrm{r,emul}}$ in (40) then becomes:

$$R_{\mathrm{r,emul}}(t) = R_{\mathrm{r,0}}\frac{1 + a_{\mathrm{Al}}(\theta_{\mathrm{IR,rotor}}(t) - \theta_{\mathrm{ref}})}{1 + a_{\mathrm{Al}}\Delta\theta} \tag{41}$$

with $\theta_{\mathrm{IR,rotor}}(t)$ being the measured rotor temperature using the IR-sensor during the temperature emulation tests and $\theta_{\mathrm{ref}} = 22$°C.

Comparing the two methods, the advantage of the first method is that no contactless IR temperature sensor needs to be mounted close to the rotor. However, using the cooldown cycles in the first method to limit the actual motor temperature increase is very time-consuming, while obtaining measurements through the second method is considerably faster due to the use of the rotor temperature measurement signal in the emulation. A mapping obtained with the first method will be referred to as a type-I mapping, while the mapping obtained with the second as a type-II mapping. The remainder of this subsection will focus on results obtained with the second method.

The results of such a measurement set of type II is shown in Fig. 7. The commanded torque setpoint varies from 31 to 35 Nm in steps of 1 Nm, and during each torque step command, the rotor temperature increase of $\Delta\theta$ is emulated by changing the rotor resistance parameter R_r in the IFOC according to (41). An artificial temperature increase ranging from $\Delta\theta = 0$°C to $\Delta\theta = 100$°C in steps of 10°C is considered. Fig. 7 shows the commanded and measured torque, the emulated rotor temperature increase $\Delta\theta$ and the measured physical temperature $\theta_{\mathrm{IR,rotor}}(t)$ of the rotor.

The measured torque corresponding to each combination of torque setpoint and emulated rotor temperature increase is averaged, interpolated and combined into a single map shown in Fig. 8*a*. Eventually 350 operating points are considered with T^* ranging from 1 to 35 Nm in steps of 1 Nm and $\Delta\theta$ ranging from 10 to 100°C in steps of 10°C. Analogously, a similar LUT has also been generated using method I but it is not shown here. However, its implementation and performance in the motor torque control are included in Fig. 9*a* and discussed in Section 5.4.

5.3 Validation of the analytical torque model

Comparing Fig. 3*c* with Fig. 8*a* shows that although the precise values of the measured torque deviations differ from the analytical model, the measured trends of torque deviation correspond to those obtained from modelling. The difference between the model and the experiment is shown in Fig. 8*b* as the relative error is expressed in percentage:

$$\epsilon\,(\%) = \left(\frac{\Delta T_{\mathrm{model}} - \Delta T_{\mathrm{meas}}}{T^*}\right)100 \tag{42}$$

Relative errors of up to 9% can be observed that are caused by a number of reasons: a slight error in the estimation of the motor parameters, especially L_r and R_{r0} and/or the actual rotor flux $\|\boldsymbol{\Psi}_r\|$ not being precisely equal to its setpoint.

We align the analytical model of torque difference with the actual by fitting an augmented model of torque difference with measured torque difference. The augmented model consists of introducing a fitting coefficient *c* in (33), resulting in

$$\frac{\Delta T_{\mathrm{model,aug}}}{T^*} = \left(\frac{\sin(2\,\mathrm{atan}(c(f/(1 + a_{\mathrm{Al}}\Delta\theta))))}{\sin(2\,\mathrm{atan}(cf))} - 1\right) \tag{43}$$

where the following cost function is used for the fitting including the emulation of different rotor temperature increases (*i*) and torque setpoints (*j*):

$$\sum_i \sum_j \left(\left.\frac{\Delta T_{\mathrm{model,aug}}}{T^*}\right|_{\Delta\theta_i, T_j^*} - \left.\frac{\Delta T_{\mathrm{meas}}}{T^*}\right|_{\Delta\theta_i, T_j^*}\right)^2 \tag{44}$$

A genetic algorithm is used for minimising (44) where $i = 1\ldots10$ and $j = 1\ldots34$, giving rise to a fitting coefficient of $c = 0.83$ for the IM under test. Referring to the definition of *f* in (34) it can be stated that physically, the fitting coefficient serves to fine-tune the motor parameter L_r.

The resulting relative error (42) with $\Delta T_{\mathrm{model,aug}}$ after fitting is shown in Fig. 8*c*. Relative errors are decreased over the entire

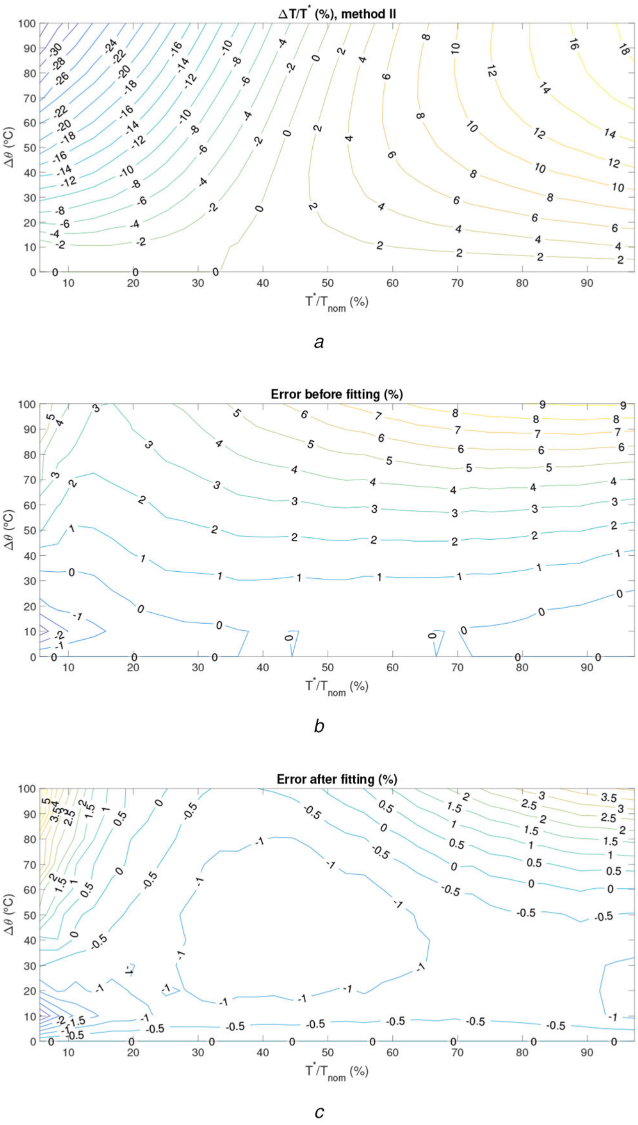

a

b

c

Fig. 8 *Experimental fitting of the analytical temperature-torque model*
(a) Experimental mapping of ΔT as a result of an emulated rotor temperature increase $\Delta\theta$ for different T^* using method II for generation of the LUT. In total, 350 operating points have been tested with T^* ranging from 1 to 35 Nm in steps of 1 Nm and $\Delta\theta$ ranging from 10 to 100°C in steps of 10°C. The nominal torque is $T_{\text{nom}} = 35.97$ Nm, ***(b)*** Relative error (42) of analytical model (33) in comparison with measurements before fitting, ***(c)*** Relative error (42) of augmented analytical model (43) in comparison with measurements after fitting

$(T^*, \Delta\theta)$ range when compared to the relative errors depicted in Fig. 8*b*.

5.4 Use of the torque mapping as a lookup table (LUT) for online temperature compensation

The torque mapping of types I and II (the latter as illustrated in Fig. 8*a*) can subsequently be used as a LUT integrated into the control algorithm to compensate for any temperature effect during operation.

A type-I LUT map was built consisting of 350 data points, with $\Delta\theta$ varying from 10 to 100°C in steps of 10°C and T^* varying from 1 to 35 Nm in steps of 1 Nm. Fig. 9*a* shows the performance of this LUT-based method included in the controller (i.e. type-I LUT is used in Fig. 5*a*) by presenting the resulting relative deviation of torque $\Delta T/T^*$. These results were obtained by carrying out performance tests using emulated rotor temperature increases according to (40). The performance of the data-driven type-I LUT was tested on 350 operating points $(T^*, \Delta\theta)$ ranging from 1.5 to 35.5 Nm for T^* in steps of 1 Nm, and $\Delta\theta$ ranging from 5 to 95°C in steps of 10°C. These are different from the points used for building type-I LUT. It can be seen that this LUT can compensate in an online fashion for temperature elevations to attain robust field-oriented torque control: the relative torque deviation is <1% in a large area of the $(T^*, \Delta\theta)$ field. Compared to Fig. 8*a* a considerable reduction in torque error is achieved with the proposed data-driven temperature compensation: implementation of the LUT in the controller results in a reduction of torque error up to 17% close to T_{nom} and up to 23% for torques lower than 20% T_{nom}.

The previously presented type-II LUT from Fig. 8*a* was additionally tested towards having online temperature compensation. The same $(T^*, \Delta\theta)$ operating points as for type-I LUT are employed for the performance tests. These points are different from those that were used for building type-II LUT. Its performance is shown in Fig. 9*b*. The performance of type-II LUT is comparable to that of type I having errors not exceeding 1% in a broad portion of the $(T^*, \Delta\theta)$ field, resulting in a robust controlled IM. Note that this type of LUT can be generated using (41) in a much faster way than type I.

The torque sensitivity of the LUT-based temperature compensation with respect to the direct measurement or indirect measurement accuracy of the rotor temperature was also investigated. Fig. 9*c* shows the resulting relative torque deviation when using type-II LUT under the same testing conditions described previously, but with a 10°C underestimation of the rotor temperature $\Delta\theta$. Compared to Fig. 4*a* the zero-deviation line is more stretched out to higher torque setpoints and the signs on either side of this line are opposite to those in Fig. 4*a* because of the use of the torque mapping as a LUT inside the control algorithm: the further away from the zero-line, the higher the torque error because of the underestimation. We have for this case a maximum deviation around 3% that can increase for larger inaccuracies of rotor temperature.

6 Conclusion

The effect of a parameter mismatch on motor torque due to a temperature increase for an IM driven by an IFOC has been investigated both analytically and experimentally. Motor heat-up during operation causes the rotor resistance to rise, which results in the incorrect estimation of both the rotor flux angular position and the angular position of the synchronous *dq*-reference frame. The controlled motor torque then no longer equals its setpoint. An analytical model has been derived, quantifying the effect of a temperature increase on angular misalignment, *dq* components of the stator current and motor torque. The derived model for torque deviation as a result of rotor temperature increase has been validated experimentally on a 5.5 kW induction motor connected to a load induction motor. Furthermore, an online, data-driven temperature compensation strategy has been implemented and experimentally verified. The advantage of a LUT-based compensation is the inherent inclusion in the table of any complex physical phenomenon that is difficult to model such as inductance variations due to magnetic saturation phenomena, largely eliminating potential model or parameter inaccuracies. The drawback, however, is the need to perform a torque measurement campaign to generate this LUT.

A data-driven lookup table was built by emulating a rotor temperature increase by adapting the rotor resistance parameter value in the controller. Ideally, the actual rotor temperature during the generation of the LUT should stay constant to have full control over temperature emulation. However, as this is not physically possible two methods are presented to circumvent this problem. A first type LUT was built by obtaining measurements in an intermittent manner where the temperature rise within the motor remains limited to a given chosen range. A second type LUT was constructed where the motor temperature rise is corrected by directly measuring the rotor temperature using a contactless IR sensor. The first method is considerably slower than the second method but does not need direct temperature measurement of the rotor. The second method on the other hand needs direct measurement of the rotor temperature but it is faster. These two types of data-driven LUTs were inserted into the online indirect field-oriented torque controller to correct for temperature increases,

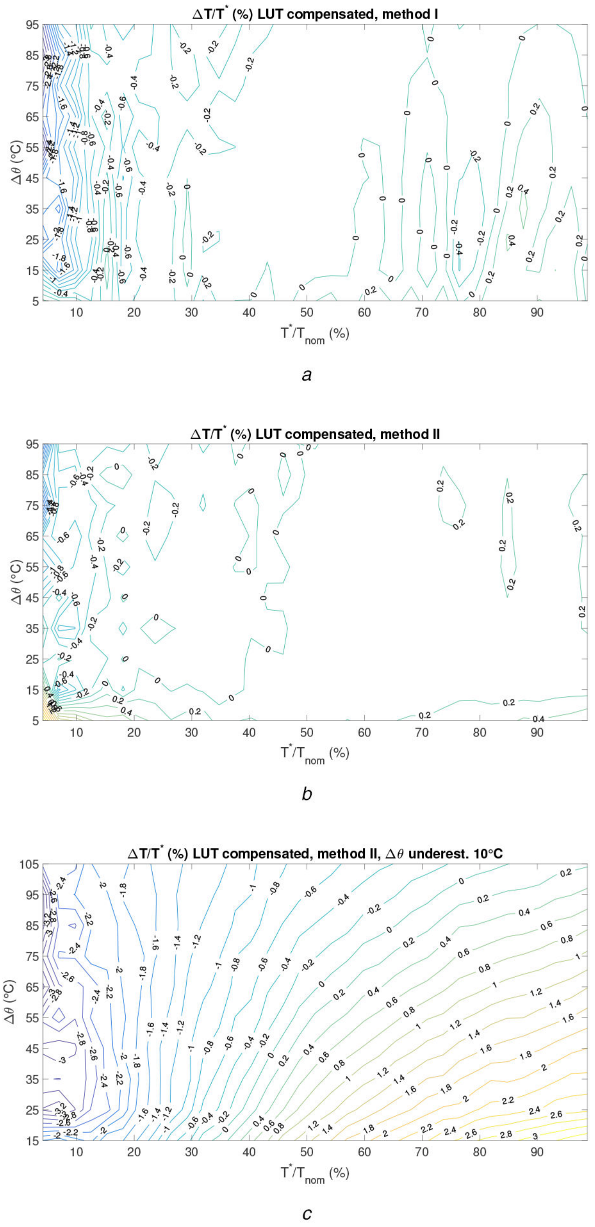

Fig. 9 *Relative deviation of torque (in %) when data-driven temperature compensation is implemented in the controller as a LUT. In total, 350 operating points have been tested, with* $\Delta\theta$ *varying from 5 to 95°C in steps of 10°C and* T^* *varying from 1.5 to 35.5 Nm in steps of 1 Nm*
(a) LUT type I, ***(b)*** LUT type II, ***(c)*** Same testing conditions and output as in (b) but with a 10°C underestimation of the rotor temperature $\Delta\theta$

and its robustness was investigated. Experimental results demonstrate the validity of the approach towards obtaining accurate indirect field-oriented torque control. A reduction of torque mismatch up to 17% at nominal torque and up to 23% at torque setpoints lower than 20% of the nominal torque is achieved, when compared to having no temperature compensation. The remaining torque error is limited to 1% in a broad operating range for both types of LUT. Finally, we investigated the effect of having inaccurate rotor temperature input to the presented data-driven method and showed in our experimental setup that a relative torque error up to 3% can occur when having an underestimation of the rotor temperature by 10°C.

7 Acknowledgment

This research was supported by the MoForM project of Flanders Make, the strategic research centre for the manufacturing industry of Flanders, Belgium.

8 References

[1] Soygenc, O., Tap, A., Ergene, L.: ‘Efficiency analysis in three phase squirrel cage induction motor’. National Conf. on Electrical, Electronics and Biomedical Engineering, Bursa, Turkey, 2016, pp. 334–338

[2] Lang, K., Muetze, A., Bauer, R., *et al.*: ‘Comparison of induction and synchronous reluctance machine based actuators for elevated temperature environments’, *IEEE Trans. Energy Convers.*, 2016, **31**, (3), pp. 1012–1022

[3] Carunaiselvane, C., Chelliah, T.: ‘Present trends and future prospects of asynchronous machines in renewable energy systems’, *Renewable Sustainable Energy Rev.*, 2017, **74**, pp. 1028–1041

[4] Finch, J.W., Giaouris, D.: ‘Controlled ac electrical drives’, *IEEE Trans. Ind. Electron.*, 2008, **55**, (2), pp. 481–491

[5] Romo, J., Adrian, M.: ‘Prediction of internal temperature in three-phase induction motors with electronic speed control’, *Electr. Power Syst. Res.*, 1997, **45**, pp. 91–99

[6] Yu, X., Dunnigan, M., Williams, B.: ‘A novel rotor resistance identification method for an indirect rotor flux-orientated controlled induction machine system’, *IEEE Trans. Power Electron.*, 2002, **17**, pp. 353–364

[7] Agamloh, E., Cavagnino, A., Vaschetto, S.: ‘Accurate determination of induction machine torque and current versus speed characteristics’, *IEEE Trans. Ind. Appl.*, 2017, **53**, (4), pp. 3285–3294

[8] Toliyat, H., Levi, E., Raina, M.: ‘A review of RFO induction motor parameter estimation techniques’, *IEEE Trans. Energy Convers.*, 2006, **18**, (2), pp. 271–283

[9] Albla, A., Brkovic, B., Jecmenica, M.: ‘Online temperature monitoring of a grid connected induction motor’, *Electr. Power Energy Syst.*, 2017, **93**, pp. 276–282

[10] Wu, Y., Gao, H.: ‘Induction-motor stator and rotor winding temperature estimation using signal injection method’, *IEEE Trans. Ind. Appl.*, 2006, **42**, (4), pp. 1038–1044

[11] Maiti, S., Chakraborty, C., Hori, Y., *et al.*: ‘Model reference adaptive controller-based rotor resistance and speed estimation techniques for vector controlled induction motor drive utilizing reactive power’, *IEEE Trans. Ind. Electron.*, 2008, **55**, (2), pp. 594–601

[12] Yang, S., Ding, D., Li, X., *et al.*: ‘A novel online parameter estimation method for indirect field oriented induction motor drives’, *IEEE Trans. Energy Convers.*, 2017, **32**, (4), pp. 1562–1573

[13] Mapelli, F., Tarsitano, D., Cheli, F.: ‘MRAS rotor resistance estimators for EV vector controlled induction motor traction drive: analysis and experimental results’, *Electr. Power Syst. Res.*, 2017, **146**, pp. 298–307

[14] Cao, P., Zhang, X., Yang, S.: ‘A unified-model-based analysis of MRAS for online rotor time constant estimation in an induction motor drive’, *IEEE Trans. Ind. Electron.*, 2017, **64**, (6), pp. 4361–4371

[15] Smith, A., Gadoue, S., Finch, J.: ‘Improved rotor flux estimation at low speeds for torque MRAS-based sensorless induction motor drives’, *IEEE Trans. Energy Convers.*, 2016, **31**, (1), pp. 270–282

[16] Wang, S., Dinavahi, V., Xiao, J.: ‘Multi-rate real-time model-based parameter estimation and state identification for induction motors’, *IET Electr. Power Appl.*, 2013, **7**, (1), pp. 77–86

[17] Bin, H., Wenlong, Q., Haifeng, L.: ‘A novel on-line rotor resistance estimation method for vector controlled induction motor drive’. The 4th Int. Power Electronics and Motion Control Conf., Xi'an, People's Republic of China, 2005, vol. 2, pp. 655–660

[18] Chiang, C.-J., Wang, Y.-K., Cheng, W.-T.: ‘EKF-based rotor and stator resistance estimation in speed sensorless control of induction motors’. American Control Conf., Montreal, QC, Canada, 2012, pp. 1174–1179

[19] Popov, N., Vukosavic, S.: ‘Estimator of the rotor temperature of induction machine based on terminal voltages and currents’, *IEEE Trans. Energy Convers.*, 2017, **32**, (1), pp. 155–163

[20] Kan, J., Zhang, K., Wang, Z.: ‘Indirect vector control with simplified rotor resistance adaptation for induction machines’, *IET Power Electron.*, 2015, **8**, pp. 1284–1294

[21] Jeon, S.H., Kim, J.-M., Jung, K.-C., *et al.*: ‘Decoupling control of bridle rolls for steel mill drive system’, *IEEE Trans. Ind. Appl.*, 1999, **35**, (1), pp. 119–125

[22] Bagheripoor, M., Bisadi, H.: ‘Application of artificial neural networks for the prediction of roll force and roll torque in hot strip rolling process’, *Appl. Math. Model.*, 2013, **37**, (7), pp. 4593–4607. Available at http://www.sciencedirect.com/science/article/pii/S0307904X12006014=0pt

[23] Bastiaensen, C., Deprez, W., Symens, W., *et al.*: ‘Parameter sensitivity and measurement uncertainty propagation in torque-estimation algorithms for induction machines’, *IEEE Trans. Instrum. Meas.*, 2008, **57**, (12), pp. 2727–2732

[24] Krishnan, R., Doran, F.C.: ‘Study of parameter sensitivity in high-performance inverter-fed induction motor drive systems’, *IEEE Trans. Ind. Appl.*, 1987, **IA-23**, (4), pp. 623–635

[25] Liu, L., Du, X., Shen, S.: ‘Indirect field-oriented torque control of induction motor considering magnetic saturation effect: error analysis’, *IET Electr. Power Appl.*, 2017, **11**, (6), pp. 1105–1113

[26] Degner, M.W., Guerrero, J.M., Briz, F.: ‘Slip-gain estimation in field-orientation-controlled induction machines using the system transient response’, *IEEE Trans. Ind. Appl.*, 2006, **42**, (3), pp. 702–711

[27] Cerruto, E., Coco, M., Consoli, A., *et al.*: ‘Rotor time constant determination of induction motor drives via steady-state torque analysis’. Proc. 7th Mediterranean Electrotechnical Conf., Antalya, Turkey, 1994, pp. 1318–1321